nature communications

Article

https://doi.org/10.1038/s41467-025-61773-3

Regulating the *N*-oxidation selectivity of P450BM3 monooxygenases for *N*-heterocycles through computer-assisted structure-guided design

Received: 12 February 2025

Accepted: 2 July 2025

Published online: 14 July 2025

Check for updates

Liu Yang[1,2,5], Zhongji Pu[3,5], Jianping Wu[1,2], Xiaofeng Liu[4], Zhe Wang[1], Haoran Yu[1,2], Liuwei Wang[1], Yan Meng[1], Gang Xu[1], Lirong Yang[1,2] & Wenlong Zheng[1,2]

N-oxidation of *N*-heterocycles is essential in the synthesis of natural products but challenging due to low efficacy and poor regioselectivity. In this study, the *N*-oxidation selective potential of P450BM3 from *Bacillus megaterium* for *N*-heterocyclic compounds is investigated. Here, twelve amino acids located in the active center, including A74, L75, V78, A82, F87, I263, A264, A328, P329, A330, I401, and L437, are investigated by site-saturation mutation. As a result, F87, A264, L75, V78, A328, I401, and L437 are identified as hotspot residues. Subsequently, the combinatorial active-site saturation test/iterative saturation mutagenesis strategy is performed. Using quinoline as a model substrate, the mutant F87G/A264G/A328L exhibits *N*-oxidation selectivity of up to 99.0%, with a conversion rate of 99.3%. Molecular dynamics simulations uncover a "push-pull" molecular mechanism elucidating the pivotal role of steric factors in determining substrate recognition and *N*-oxidation selectivity. This study provides an efficient *N*-oxide synthesis method and insights into P450BM3's molecular mechanisms.

The *N*-oxidation of *N*-heterocyclic compounds represents a significant reaction in organic chemistry, given that the resulting motifs have been effectively utilized in the synthesis of various pharmaceuticals possessing anticancer, antibacterial, and anti-inflammatory properties[1–4] (Fig. 1a). However, achieving highly *N*-oxidation selectivity of *N*-heterocyclics remains a challenge in the field of synthetic chemistry[5,6].

Chemical methods for *N*-oxidation of *N*-heterocyclics commonly relied on reductive cyclization of laboriously constructed nitro-compounds[5,7–9]. Okuma et al.[8] investigated the reductive cyclization of 3-hydroxy-3-(2-nitrophenyl)−1-p-tolylpropan-1-one to synthesize the corresponding quinoline *N*-oxide, achieving an 80% yield under harsh reaction conditions. However, the production of a significant amount of by-products was inevitable. The harsh reaction conditions and the challenging catalyst separation led to the method's inefficiency and environmental unfriendliness. Furthermore, the direct oxidation of heterocyclic scaffolds for the preparation of *N*-oxides is also widespread[10]. Traditional synthetic routes for the direct nitrogen oxidation of heterocyclic compounds typically rely on costly catalyst-mediated peroxide oxidation[11–14]. Hydrogen peroxide and *m*-chloroperoxybenzoic acid are commonly utilized as oxidizing agents in nitrogen oxidation reactions. However, the oxidants decompose easily at elevated temperatures and by-products such as *m*-chlorobenzoic acid increase the difficulty of separation[15,16]. Additionally, the use of

[1]Institute of Bioengineering, College of Chemical and Biological Engineering, Zhejiang University, Hangzhou 310058, China. [2]ZJU-Hangzhou Global Scientific and Technological Innovation Centre, Zhejiang University, Hangzhou 311215, China. [3]Xianghu laboratory, Hangzhou 311231, China. [4]Shaoxing Institute, Zhejiang University, Shaoxing 312000, China. [5]These authors contributed equally: Liu Yang, Zhongji Pu. e-mail: per@zju.edu.cn

https://doi.org/10.1038/s41467-025-61773-3

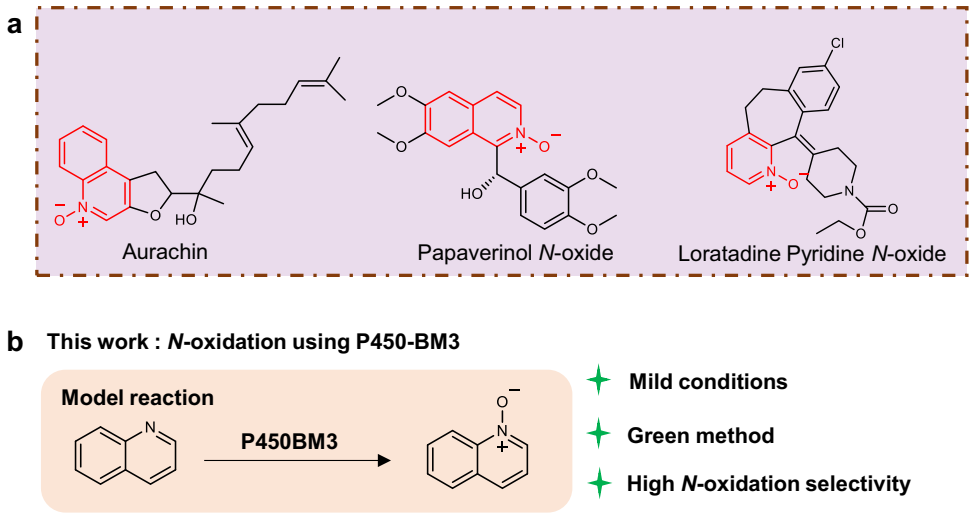

Fig. 1 | Application of *N*-heterocyclic oxides in pharmaceuticals and the model reaction investigated in this work. a Representative examples of drug molecules containing *N*-heterocyclic oxides: Aurachin, Papaverinol *N*-oxide, and Loratadine Pyridine *N*-oxide. **b** Model reaction for *N*-oxidation using P450BM3.

costly catalysts, such as methyltrioxorhenium, leads to Re–C bond cleavage, which diminishes catalytic activity and impedes catalyst recycling[17]. Recent advancements in peroxide oxidation methods have been documented, yet they frequently necessitate the incorporation of hazardous agents like tellurium or tungsten. Larionov et al.[12] have successfully developed an optimized molybdenum (VI)-catalyzed *N*-oxidation system that effectively replaces the need for tellurium or tungsten in the oxidation of *N*-heterocycles, with quinoline *N*-oxides exhibiting a regioselectivity of 99%. However, this reaction is conducted in an acetonitrile solvent system, and the costly catalyst is used at 10 mol% relative to the substrate, which diminishes the economic viability and environmental sustainability of the process. Hence, the development of more efficient, environmentally sustainable, and cost-effective chemical methods for achieving highly *N*-oxidation selective represents a pressing challenge.

Biocatalytic technology has become one of the hot research fields due to its remarkable characteristics of environmental friendliness, process efficiency and sustainable development. While, there is still lack of efficient and feasible bio-methodologies for achieving highly selective *N*-oxygenation of *N*-heterocycles. John B. Sutherland attempted a biological oxidation method using *Cunninghamella elegans* incubated in Sabouraud medium with 1.9 mM quinoline and isoquinoline for 7 days. However, the selectivity of quinoline and isoquinoline *N*-oxides were only 65% and 3%, respectively[18]. Previous reports have indicated that certain P450 enzymes, including CYP2E1, 2A6, 1A2, Cam, and 3A4, can metabolize quinolines or isoquinoline to the corresponding *N*-oxide[19–23]. However, regioselectivity and activity of these enzymes are unsatisfactory. Among these enzymes, CYP3A4 exhibits the highest production of quinoline *N*-oxide, with a regioselectivity of 80%. However, both the *N*-oxidation rate and substrate concentration are quite low, at 1.79 μmol/μmolP450/min and 0.5 mM, respectively[21]. Furthermore, Balázs Pogrányi et al.[24] tested the oxidation of *N*-heterocyclics using the unspecific peroxygenase (rAaeUPO-PaDa-I-H). The results showed that the regioselectivity of isoquinoline *N*-oxide and dihydroxy compounds was only 34% and 20%, respectively, and no quinoline *N*-oxide was produced. Although these biocatalytic methods are promising in terms of environment friendly, they suffer from either low *N*-oxidation selectivity or activity. Therefore, it is of utmost necessity and significance to develop a highly selective, efficient and environmentally friendly method for synthesizing *N*-oxides of *N*-heterocycles.

P450BM3, derived from *Bacillus megaterium*, is renowned for its efficiency hydroxylation of oxidative C-H bonds[25,26]. Its remarkable flexibility, self-sustaining electron transfer system, and ability to achieve regioselective oxidation at specific positions make it highly valuable for challenging oxygenation reactions that are difficult to accomplish using conventional chemical methods[27–33]. Reetz et al.[34] pioneered the achievement of highly regioselective sulfur atom oxidation by modifying the active pockets of P450BM3, resulting in the acquisition of the WAJ-9 (L75F-F87L-A328F) mutant. This mutant demonstrated exceptional catalytic performance, producing sulfoxide (*S*)- and (*R*)- with an enantiomeric ratio of 92:8 in the oxidation of thiochromanone. Additionally, P450BM3 also exhibit improved regioselectivity for hydroxylation reactions involving aromatic hydrocarbons[35,36], short-chain alkanes[37–39], and steroids[40–42]. Li et al.[28]successfully engineered a series of P450BM3 mutants with enhanced regioselectivity (91–99%) for the *p*-hydroxylation of *m*-alkylphenols by reshaping the substrate binding pocket and access channel. This modification led to the efficient production of valuable *m*-alkylbenzene-1,4-diols with high conversion rates ranging from 95% to 99%. However, although P450BM3 demonstrates broad substrate promiscuity and high regioselective oxidation capabilities, the wild-type P450BM3 lacks *N*-oxidation activity for *N*-heterocycles.

In this research, we selected P450BM3 as the target enzyme and used quinoline as a molecular probe to develop *N*-oxidation capability and elucidate the *N*-oxidation selectivity mechanism of P450BM3 (Fig. 1b). Informed by molecular dynamics (MD) simulations, we investigated how the steric hindrance at P450BM3's active center influenced the *N*-oxidation selectivity. Employing structure-guided directed evolution, we successfully generated mutants that exhibit high *N*-oxidation selectivity in *N*-heterocycles. Additionally, MD simulations provided insights into the molecular basis of substrate recognition and *N*-oxidation selectivity in P450BM3. This study is significant as it delivers an efficient synthesis approach for *N*-heterocyclic *N*-oxides and broadens the application scope of P450BM3.

Results and discussion

Steric hindrance in active center impedes P450BM3 *N*-oxidation

The cytochrome P450BM3 enzyme, a versatile catalyst native to *Bacillus megaterium*, has been extensively studied for its ability to catalyze a broad range of oxidative reactions, including hydroxylation, epoxidation, and carbene transfer. However, it is noteworthy that prior to recent advancements, the capability of P450BM3 for catalyzing *N*-oxidation of *N*-heterocyclics had not been reported. Our preliminary investigations revealed that the wild-type (WT) enzyme does not exhibit any significant *N*-oxidation activity. Structure-based rational

https://doi.org/10.1038/s41467-025-61773-3

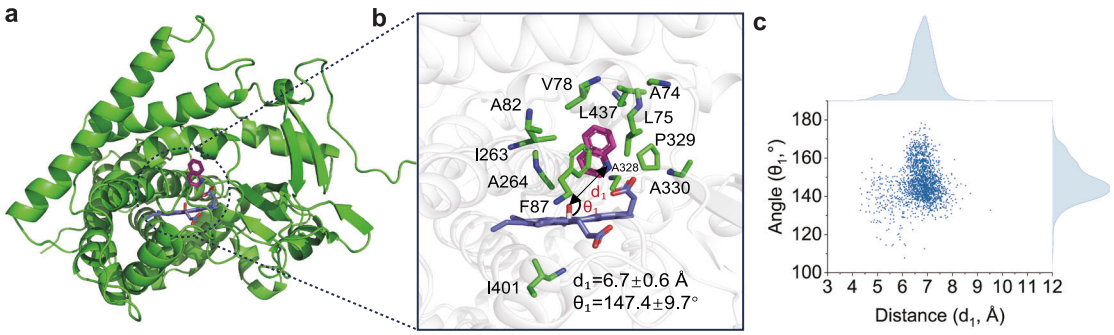

Fig. 2 | Model of wild-type P450BM3 with the docked ligands. a Structure of P450BM3 (PDB ID:1JPZ) with quinoline as ligand. **b** Amino acid residues located at the binding pocket. **c** Distance and angle fluctuations of quinoline nitrogen atom relative to heme-O of WT from the classic MD simulations. Note: "d_1" stands for distance between quinoline nitrogen atom and heme oxygen atom (heme-O); "θ_1" stands for the angle between quinoline nitrogen atom and heme iron atom (heme-Fe=O).

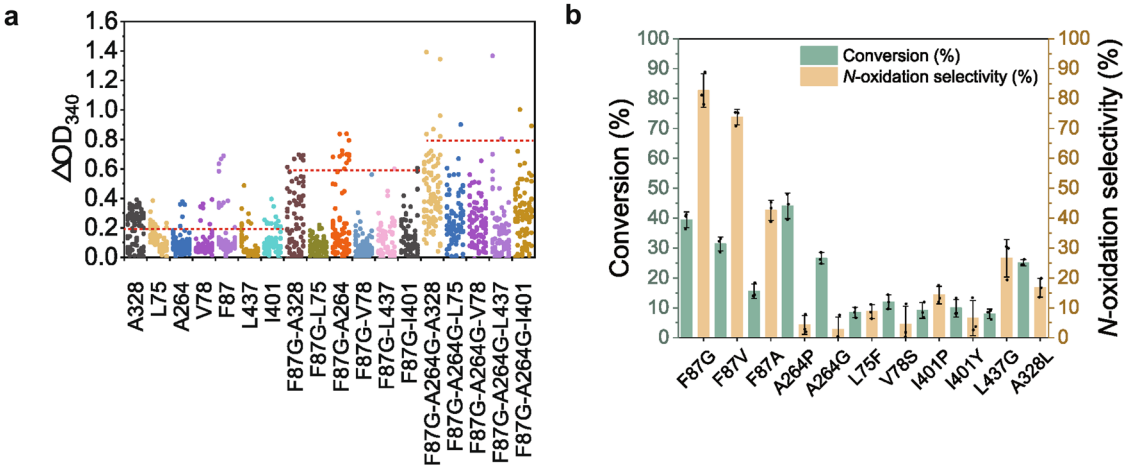

Fig. 3 | Directed evolution of P450BM3 for *N*-oxidation of *N*-heterocycles. a Mutant library screening. The reactions were conducted in a 96-well plate, with each well containing 200 μL a K_2HPO_4/KH_2PO_4 buffer (50 mM, pH 8.0) with quinoline (1 mM), crude enzyme solution (100 μL), 1 mM NADPH, and was incubated at 30 °C for 10 min. The absorbance at 340 nm (OD_{340}) was then measured. The red line indicates the threshold used for the selection of mutants for further characterization. 96 variants are tested in per site, $n = 96$ independent experiments. Source data are provided as a Source Data file. **b** Conversion and *N*-oxidation selectivity of the positive mutants in site-directed saturation mutations determined by HPLC. The reactions were carried out in 1.5 mL Eppendorf tubes, each containing 1 mL of a K_2HPO_4/KH_2PO_4 buffer with quinoline (1 mM), crude enzyme (960 μL), and 2 mM NADPH. The reactions were incubated at 30 °C for 16 h. Reactions were conducted in three independent biological experiments ($n = 3$). The data are presented as mean values ± SD across three independent repetitions. Error bars indicate the standard deviation of the replicate measurements, with the error bar centers representing the means of these replicates. Replicate measurements are depicted as block circles. The source data are provided in a Source Data file.

design has proven to be an effective approach for expanding the reaction diversity of P450BM3[27,28]. In this study, structure-based protein engineering was performed to broaden the functionality of P450BM3 towards *N*-heterocyclic *N*-oxidation. The conversion of quinoline to quinoline *N*-oxide was utilized as a model reaction.

First, we conducted molecular docking studies with quinoline as the model substrate, utilizing the X-ray crystal structure of P450BM3 (PDB ID: 1JPZ) as the receptor (Fig. 2a). Subsequently, 100 ns MD simulations was conducted, and the conformations with the converged root-mean-square deviation (RMSD) were selected for analysis. As depicted in Fig. 2b, the active center of P450BM3 is composed of several key amino acid residues including A74, L75, V78, A82, F87, I263, A264, A328, P329, L437 and A330. It is well known that the type, geometric structure, and microenvironment of the residues in active center play a crucial role in defining the catalytic properties of the enzyme[43–45]. Hence, we speculated that the geometry and microenvironment of P450BM3's active center may not be optimal for catalyzing quinoline *N*-oxidation. The MD simulation results supported our hypothesis, showing that certain amino acid residues, such as Phe87, occupy a position between the iron center and the substrate, creating a potential steric hindrance effect[46]. As a result, quinoline was observed to be unable to stably approach the active center. Furthermore, the distance between the nitrogen atom of the quinoline and the heme-O was measured, with the average distance exceeding 6.7 Å (Fig. 2c), suggesting that nitrogen oxidation of quinoline is difficultly to occur. Based on these observations, we proposed that the amino acid residues composing the active center generate steric hindrance, thereby hindering the ability of P450BM3 to oxidize the nitrogen atom of quinoline. Guided by the hypothesis, we selected 11 amino acid residues constituting the active center for further investigation, including A74, L75, V78, A82, F87, I263, A264, A328, P329, A330, and L437. In addition, I401, located beneath the heme ring, was also included in the analysis, as previous studies have shown that the incorporation of cyclic amino acids at this site can effectively promote the proximity of the heme group to the substrate[47–49].

Regulating the *N*-oxidation capability of P450BM3 by semi-rational design

Initially, twelve residues were targeted for site-directed saturation mutagenesis using the degenerate codon NNK[50], aiming to identify positions contributing to the oxidative activity toward quinoline. As shown in Fig. 3a, a total of 1152 mutants were generated (12 sites × 96

https://doi.org/10.1038/s41467-025-61773-3

Table 1 | Products distribution of quinoline catalyzed by mutants of P450BM3

Mutants	*Conv.*[a] (%)	*N*-oxidation *sele.*(%)	5-OH *sele.*(%)	3-OH *sele.*(%)	Others[b] (%)
F87G	39.4	82.7	4.8	1.1	11.4
F87V	31.3	73.8	5.6	2.5	18.1
F87A	15.6	42.6	16.5	n.d.	40.9
F87G/A264G	64.4	92.7	3.7	n.d.	7.3
F87G/A264G/A328L	68.2	98.5	n.d.	n.d.	1.5

5-OH 5-hydroquinoline, 3-OH 3-hydroquinoline. '*sele.*' represents *regio*selectivity, and '*conv.*' represents conversion of substrate. Reactions were conducted in three independent experiments ($n = 3$).
[a]Reaction conditions: 1 mM quinoline in 1 mL K_2HPO_4/KH_2PO_4 (50 mM) buffer pH 8.0 for 16 h, 220 rpm, 30 °C.
[b]Unknown compounds.

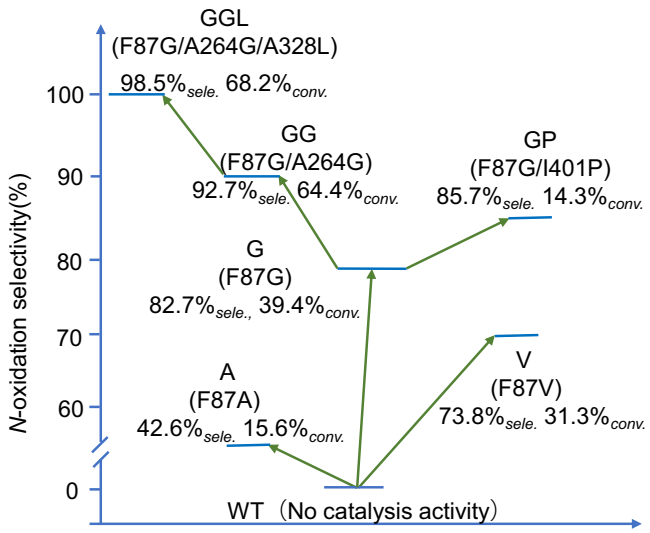

Fig. 4 | Directed evolution of P450BM3 for *N*-oxidation of *N*-heterocycles. Directed evolution and characterization of mutants with enhanced *N*-oxidation selectivity. The reactions were carried out in 1.5 mL Eppendorf (EP) tubes, each containing 1 mL of a K_2HPO_4/KH_2PO_4 buffer solution (50 mM, pH 8.0) with quinoline (1 mM), crude enzyme (960 μL), and 2 mM NADPH. The reactions were incubated at 30 °C for 16 h. Note: '*sele.*' stands for *N*-oxidation selectivity, and '*conv.*' stands for conversion. Reactions were conducted in three independent experiments ($n = 3$). The source data are provided in a Source Data file.

variants per site) and screened, among which only a small subset exhibited enhanced catalytic activity compared to the wild-type enzyme. These positive mutants were predominantly localized at the sites of L75, V78, F87, A264, A328, I401, and L437. Variants that showed no detectable activity during the primary screening were excluded from subsequent analysis.

Excitingly, high-performance liquid chromatography (HPLC) analysis confirmed that several mutants, including L75F, V78S, F87G, A264P, I401P, A328L, and L437G, exhibited *N*-oxidation activity. The *N*-oxidation selectivities of these mutants were determined to be 8.7%, 4.5%, 82.7%, 4.3%, 14.3%, 16.7%, and 26.6%, respectively (Fig. 3b). In addition, three advantageous mutants were obtained at position 87, namely F87G, F87V, and F87A. They exhibited *N*-oxidation activities of 0.84 μmol/μmol P450/min, 0.70 μmol/μmol P450/min and 0.40 μmol/μmol P450/min, respectively. The *N*-oxidation selectivities of the three mutants were 82.7%, 73.8%, and 42.6%, respectively (Fig. 3b and Supplementary Table 1). Notably, some of these residues have been the focus of previous studies exploring the regioselective modification of P450BM3 for other non-natural substrates such as hexane, indole and 4-Nitrophenol. For instance, F87 has been proven to play a critical role in influencing substrate specificity and regulating enzymatic activity[46,51,52]. Additionally, residues such as L75, V78, A328, and I401 have been reported to significantly contribute to reshaping the active center, thereby enhancing catalytic efficiency against acyclic terpenes geranyl- or nerylacetone and fluoreneor improving regioselectivity[48,53]. Mutations at these positions can alter the geometry and microenvironment of the active center, thereby expanding the functional diversity of the enzyme.

Improving *N*-oxidation selectivity of P450BM3 by CAST/ISM strategy

Although positive residues influencing the *N*-oxide activity of P450BM3 have been identified, the *N*-oxidation selectivity of these single-point mutants remains suboptimal. Therefore, we performed the combinatorial active-site saturation test/iterative saturation mutagenesis (CAST/ISM) strategy on L75, V78, F87, A264, I401, A328, and L437 to generate mutants with improved *N*-oxidation selectivity[54,55]. Initially, the F87G mutant was selected as the starting strain for further directed evolution due to its superior *N*-oxidation selectivity and conversion rates of 82.7% and 39.4%, respectively. Meanwhile, hydroxylation by-products such as 3-hydroxyquinoline and 5-hydroxyquinoline products were detected. The quantitative data are shown in Table 1. As shown in Fig. 4 and Supplementary Fig. 1, the double mutants F87G/I401P and F87G/A264G exhibited enhanced *N*-oxidation selectivity, increasing from 82.7% to 85.7% and 92.7%, respectively, with corresponding conversion rates of 14.3% and 64.4%. Among these, the F87G/A264G mutant showed the best performance in both *N*-oxidation selectivity and conversion, and was therefore selected for further evolution in quinoline *N*-oxidation. In the third round of combinatorial mutagenesis, the F87G/A264G/A328L mutant exhibited impressive *N*-oxide selectivity of 98.5% and a conversion rate of 68.2%. However, when F87G/A264G/A328L was used as the starting strain for further combinatorial mutations, the resulting four-point mutants either lacked catalytic activity or exhibited reduced *N*-oxidation selectivity. So, further combinatorial mutagenesis was discontinued. In summary, after several rounds of iterative combinatorial mutagenesis, the F87G/A264G/A328L mutant exhibited the best performance in quinoline *N*-oxidation.

The kinetic constants of the F87G/A264G/A328L mutant were determined. The K_m, k_{cat}, and k_{ca}/K_m values were found to be 0.31 mM, 9.74 min^{-1}, and 31.41 mM^{-1} min^{-1}, respectively. Notably, the rate of quinoline *N*-oxide formation reached 4.37 μmol/μmolP450/min, which is 2.4 times higher than that of CYP3A4[21]. Additionally, NADPH utilization significantly increased from 7.5% to 22.3% (as shown in Supplementary Table 1 and Supplementary Fig. 4). Given that the wild-type P450BM3 does not exhibit catalytic activity for the *N*-oxidation of *N*-heterocycles, the F87G/A264G/A328L mutant represents a significant breakthrough, achieving *N*-oxidation activity from scratch.

Exploring the *N*-oxygenation potential of P450BM3 mutants for different *N*-heterocycles

The directed evolution of P450BM3 yielded a valuable mutant library with variations in the active center geometry and microenvironment, suggesting that these mutants may possess the potential to catalyze the *N*-oxidation of other *N*-heterocyclic compounds. To investigate this, we tested a range of *N*-heterocyclic substrates, including quinolines, isoquinolines, and pyridines, and mapped the *N*-oxidation selectivity and conversion profiles of the mutants against these substrates (Fig. 5).

https://doi.org/10.1038/s41467-025-61773-3

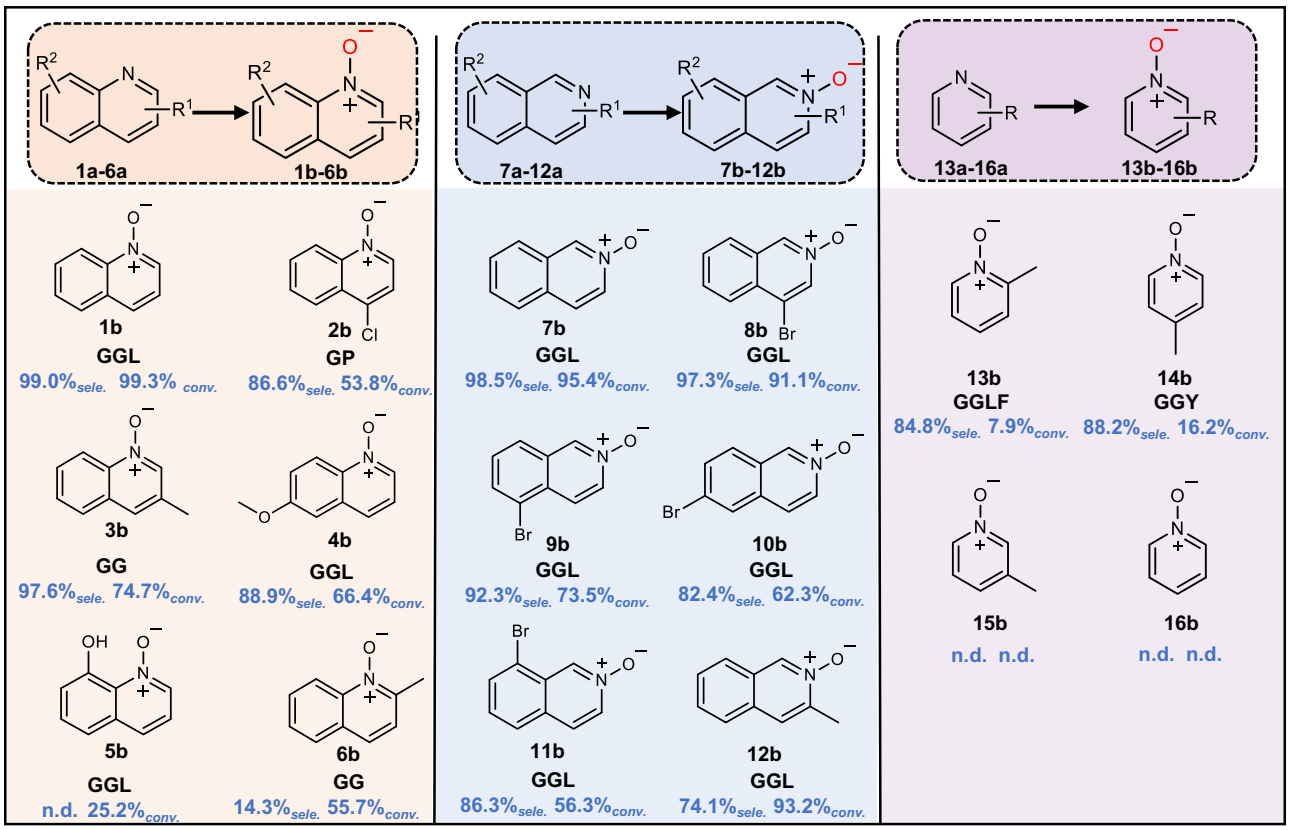

Fig. 5 | *N*-oxidation of various *N*-heterocycles catalyzed by different p450BM3 mutants. Reaction condition (2 mL): 1a -16a (1 mM), 0.5 μM enzymes and 2 mM NADPH in K_2HPO_4-KH_2PO_4 buffer (50 mM, pH 8.0). Reactions were incubated at 30 °C for 16 h; Note: '*sele.*' stands for *N*-oxidation selectivity, and '*conv.*' stands for conversion. n.d.: not detected. Three independent biological experiments were conducted ($n = 3$). Source data are provided as a Source Data file.

Among the mutants, the F87G/A264G/A328L variant (GGL) demonstrated outstanding *N*-oxidation selectivity (92.3–99.0%) and high substrate conversion rates (73.5–99.3%) for compounds 1a, 7a, 8a, and 9a. For compounds 4a, 10a, and 11a, GGL exhibited moderate *N*-oxidation selectivity, exceeding 80%. In addition, the F87G/A264G variant (GG) showed outstanding *N*-oxidation selectivity of 97.6% for 3a, with a conversion rate of 74.7%. The F87G/I401P (GP) mutant achieved 86.6% *N*-oxidation selectivity and a conversion rate of 53.8% for 2a. While the F87G/A264G/A328L/Y51F (GGLF) mutant exhibited 84.8% *N*-oxidation selectivity, but with a low conversion rate of 7.9% for 13a. The F87G/A264G/I401Y (GGY) mutant exhibited 88.2% *N*-oxidation selectivity, but with a low conversion rate of 16.2% for 14a. Interestingly, none of the mutants tested were able to produce 5b from 5a, although some substrate consumption was observed. We hypothesize that the hydroxyl group adjacent to the nitrogen atom may hinder its proximity to the activated Fe=O center. Additionally, for pyridine compounds, most of them exhibited low conversion rates or no activity, as seen with compounds 15a and 16a. This could be attributed to the small size of the pyridine ring, which may not favorably position it within the enzyme's active center.

It is important to note that no single mutant exhibited optimal *N*-oxidation activity across all tested substrates, a limitation arising from the specific binding conformations of the substrates within the enzyme. However, mutants exhibiting improved activity for different substrates offer a promising pathway for further optimization through rational protein engineering. In summary, this study highlights the potential of engineered P450BM3 variants for the efficient *N*-oxidation of *N*-heterocyclic compounds, including quinolines and pyridines. While further optimization is required to enhance substrate conversion and regioselectivity for specific compounds, these results provide a solid foundation for future work.

MD simulations reveal "push-pull" mechanisms influencing substrate recognition and *N*-oxidation selectivity

MD simulations were conducted using models of wild-type P450BM3, mutants F87G and F87G/A264G/A328L complexed with ligands to investigate the mechanisms underlying substrate recognition and *N*-oxidation selectivity. The MD simulations results revealed a distinct binding orientation of quinoline in the wild-type enzyme active center. The phenylalanine residue at position 87 adopted a conformation perpendicular to the benzene ring of quinoline and formed a T-shaped π-π stack with quinoline (Fig. 6a, and Supplementary Fig. 7a). This configuration imposed steric hindrance, thereby preventing quinoline from approaching the heme-O group.

The mean distance (d_1) between the nitrogen atom of quinoline and the oxygen atom of the heme-O group was 6.7 ± 0.6 Å, a distance insufficient to support efficient *N*-oxidation. Substituting phenylalanine with glycine (F87G mutation) alleviated this steric hindrance, reducing d_1 to 5.5 ± 0.7 Å and improving access to the heme group (Figs. 6b and 7a). As a result, the F87G mutation conferred *N*-oxidation activity towards quinoline, which was absent in the wild-type enzyme, highlighting the critical role of residue F87 in alleviating steric hindrance and enabling substrate access to the catalytic center (Fig. 7b). Further analysis of the F87G-quinoline complex model showed the ligand positioned between residues A264 and A328, suggesting that additional mutations at these positions could potentially regulate the orientation of quinoline within the active center, thereby optimizing the *N*-oxidation process. Subsequent mutations, including A328L and A264G, further refined quinoline's binding pose (Fig. 6c). In the GGL mutant, d_1 was further reduced to 5.2 ± 0.5 Å, while the angle (θ_1) between the heme-Fe=O group and the quinoline nitrogen atom decreased from 147.4 ± 9.7° to 122.6° ± 6.2° (Fig. 6c), in agreement with previous research that the optimal angle for *N*-oxidation is around

https://doi.org/10.1038/s41467-025-61773-3

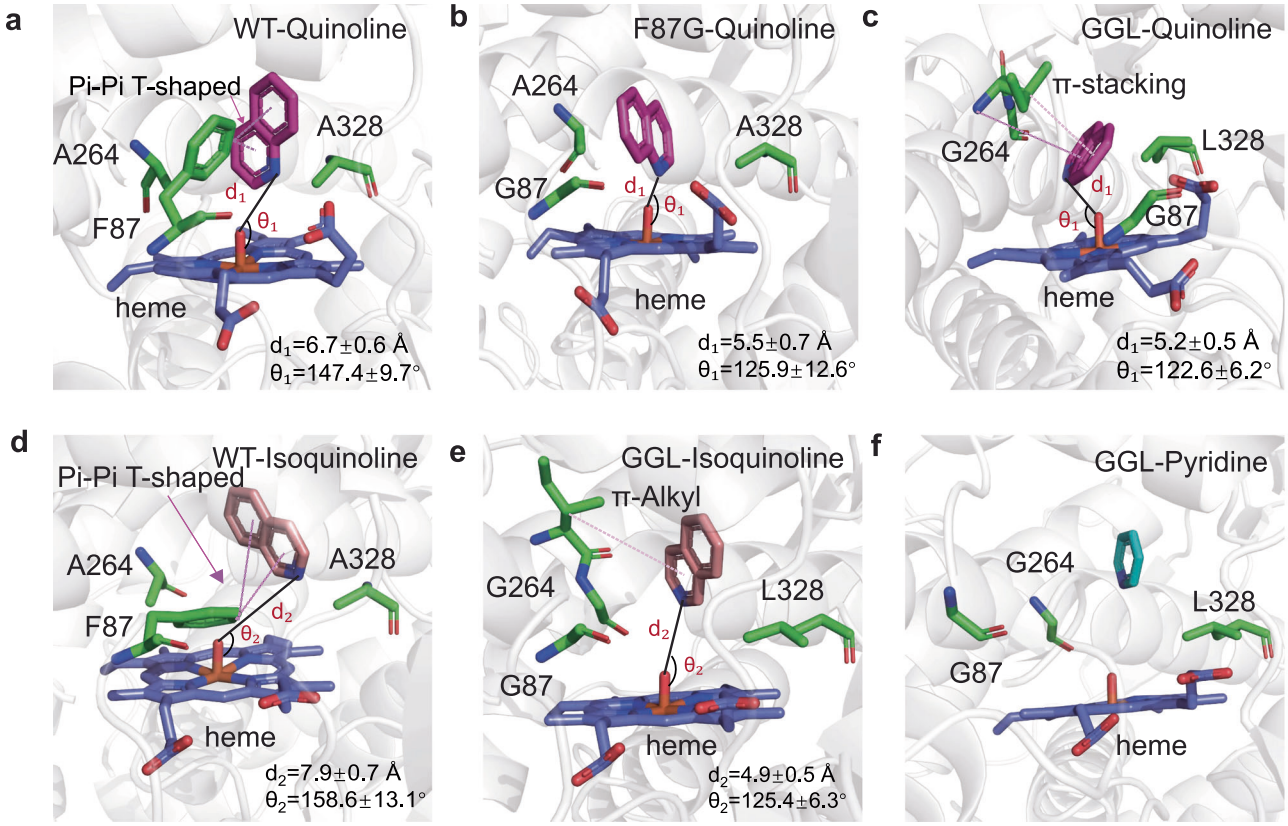

Fig. 6 | Interaction between ligands and amino acid residues in the active site of P450BM3 and its mutants. a Interaction between quinoline and amino acid residues in the active center of wide-type P450BM3. **b** Interaction between quinoline and amino acid residues in the active center of F87G mutant. **c** Interaction between quinoline and amino acid residues in the active center of GGL mutant. **d** Interaction between isoquinoline and amino acid residues in the active center of wide-type P450BM3. **e** Interaction between isoquinoline and amino acid residues in the active center of GGL mutant. **f** Interaction between pyridine and amino acid residues in the active center of GGL mutant. Note: "d" stands for distance between the nitrogen atom of sunstrate and the oxygen atom of the heme-O group; "θ" stands for the angle between the nitrogen atom of substrate and heme-Fe=O.

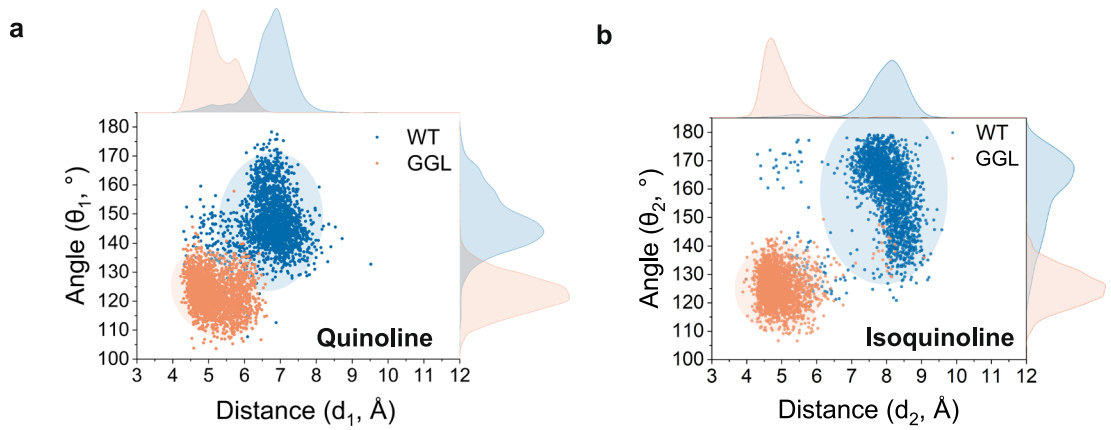

Fig. 7 | Statistics of distance and angle between nitrogen atom and heme-O. a Statistical analysis of distances nitrogen atom of quinoline and the oxygen atom of the heme-O (d_1) and the angle between the nitrogen atom of quinoline and heme-Fe=O (θ_1) derived from the 20 ns convergent trajectories. **b** Statistical analysis of distances nitrogen atom of isoquinoline and the oxygen atom of the heme-O (d_2) and the angle between the nitrogen atom of isoquinoline and heme-Fe=O (θ_2) derived from the 20 ns equilibrated trajectories. Note: "d" stands for distance between the nitrogen atom of substrate and the oxygen atom of the heme-O group; "θ" stands for the angle between the nitrogen atom of substrate and heme-Fe=O. Source data are provided as a Source Data file.

110–130°, which would provide a good orbital overlap and reduce the activation barrier[56]. Moreover, the mean binding energy of the mutant GGL was −16.98 ± 0.08 kcal/mol calculated by MM/GBSA method, which was lower than that of the wild type (−15.75 ± 0.48 kcal/mol) (Supplementary Table 2). These changes facilitated a near-attack conformation, greatly enhancing the efficiency of quinoline *N*-oxidation.

Furthermore, a "push-pull" hypothesis was proposed to describe the substrate recognition and *N*-oxidation selectivity mechanism of P450BM3 (Fig. 8). In the model GGL, the A328L mutation introduces a nonpolar residue with a longer side chain, effectively "pushing" the substrate closer to the heme-Fe=O group. Simultaneously, the A264G mutation reduces steric hindrance and enables the residues of I263 to

https://doi.org/10.1038/s41467-025-61773-3

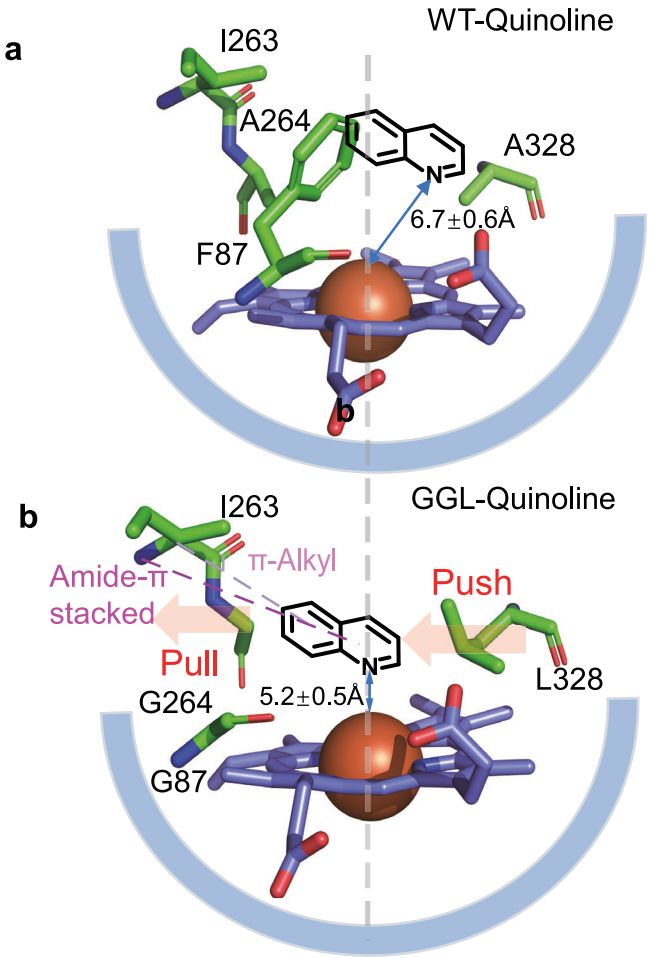

Fig. 8 | The "push-pull" model influencing substrate recognition and *N*-oxidation selectivity in P450BM3. a The model of quinoline as the substrate with WT. **b** The model of quinoline as the substrate with mutant F87G/A264G/A328L (GGL).

form π-stacking interactions (amide-π stacked and π-alkyl) with quinoline's aromatic pyridine ring (Fig. 6c and Supplementary Fig. 7b), which plays a crucial role in the binding affinity between the protein and ligand[57], pulling the substrate into the optimal catalytic orientation. The "push-pull" mechanism was also evident in simulations with isoquinoline as a substrate. Steric effects from L328, combined with a π-alkyl interaction between I263 and the pyridine ring of isoquinoline, facilitated the "push-pull" interaction, effectively positioning isoquinoline in its optimal catalytic conformation. In the wild-type enzyme, the mean distance (d_2) between the nitrogen atom of isoquinoline and the heme-O was 7.9 ± 0.7 Å, with a mean angle (θ_2) of 158.6° ± 13.1° (Fig. 6d and Supplementary Fig. 7c). The steric hindrance caused by π-π interactions with residue F87 obstructed the substrate's approach to the heme-Fe=O group. In the GGL mutant, d_2 decreased to 4.9 ± 0.5 Å, and θ_2 decreased to 125.4° ± 6.3° (Figs. 6e, Fig. 7b and Supplementary Fig. 7d). Moreover, mean binding energy of the GGL was −16.78 ± 0.06 kcal/mol, which was lower than that of the wild type with isoquinoline as a ligand (−14.34 ± 0.27 kcal/mol) (Supplementary Table 2).

The mutants' deficiency in catalyzing pyridine *N*-oxidation was further explored. Docking model of GGL variant indicated an unfavorable catalytic conformation, evidenced by an increased the nitrogen atom of pyridine and the heme-O distance (Fig. 6f). This is likely due to the mutant's enlarged active center cavity, which was unable to properly position the small pyridine molecule for efficient oxidation. We also performed MD simulations on GGL variant using 5a as ligand. The simulation data revealed hydrogen bond formation between the heme-O and the hydroxyl group of the substrate, with a mean distance of 2.85 Å and a mean angle of 146.69°. The frequency of hydrogen bond formation was 32.94% (defined by $d_3 < 4$ Å, $120° < \theta_3 < 180°$)[58]. The hydrogen bonding interaction stabilizes a specific conformation of the substrate thereby preventing the formation of the nitrogen oxidation product 5b (Supplementary Fig. 8). These observations are consistent with the experimental data, which showed no detectable activity with pyridine substrates. Moreover, the physicochemical properties of substituent groups on *N*-heterocycles significantly influenced substrate conformations in the enzyme active center, resulting in variations in substrate recognition and *N*-oxidation selectivity (Fig. 5).

Scale-up reaction for preparation of *N*-oxidation with P450BM3 mutant

To further assess the application potential of P450BM3 mutants, scale-up reaction for preparation of *N*-heterocycles was carried out using the F87G/A264G/A328L variant in a 50 mL reactor with a substrate concentration of 3 mM. A GDH-glucose-based cofactor regeneration system was employed to maintain a continuous supply of NADPH. The reaction progress was monitored through HPLC analysis. As shown in Fig. 9a, after 6 h of reaction, the conversion rate of quinoline (1a) reached 96.4% and exceed 99.3% after 10 h, with residual substrate levels falling below the detection limit of HPLC (Fig. 9b). The *N*-oxidation selectivity for quinoline exceeded 99.0%. By means of the separation procedures involved in the " Preparation of *N*-Oxidation of *N*-Heterocycles " section of the supplementary information, the isolated yield of quinoline-*N*-oxide was 83.6% (16.2 mg). Isoquinoline and 4-bromoisoquinoline were subsequently selected as additional substrates for scale-up reactions. As illustrated in Fig. 9c and 9d, after 10 h of reaction, the *N*-oxidation conversion rates for isoquinoline (7a) and 4-bromoisoquinoline (8a) reached 95.6% and 92.5%, respectively, with excellent *N*-oxidation selectivities of 98.0% and 97.1%. The isolated yields were 76.4% (14.8 mg) and 64.4% (20.1 mg), respectively. These *N*-oxidation products are important intermediates for anti-inflammatory alkaloids[59]. These findings underscore the capability of the engineered P450BM3 enzyme to perform green and efficient *N*-oxidation of *N*-heterocycles, highlighting its potential for sustainable preparative-scale synthesis and broad applicability in industrial biocatalysis.

In conclusion, achieving *N*-oxidation selectivity of *N*-heterocycles remains a significant challenge in organic synthesis. The enzyme P450BM3 from *Bacillus megaterium* has garnered considerable attention due to its broad substrate promiscuity and catalytic versatility. Molecular docking and MD simulations revealed that steric hindrance within the enzyme's active center plays a crucial role in both substrate recognition and *N*-oxidation selectivity. To investigate this, 12 key amino acids located in the active center were rationally selected to construct a mutant library. Then, CAST/ISM directed evolution strategy was employed to generate mutants with enhanced *N*-oxidation selectivity of *N*-heterocycles. Among the resulting mutants, the F87G/A264G/A328L variant displayed over 99.0% *N*-oxidation selectivity and greater than 99.3% substrate conversion when quinoline was used as the substrate, in contrast to the wild-type enzyme, which showed no detectable activity. Several other mutants also exhibited exceptional *N*-oxidation activity toward a variety of *N*-heterocyclic compounds, including quinolines, isoquinolines, and pyridines. Insights gained from MD simulations further elucidated the substrate binding and *N*-oxidation selectivity mechanisms, leading to the development of a "push-pull" model. This model suggests that steric hindrance within the enzyme's active center play a pivotal role in *N*-heterocycle recognition and the *N*-oxidation selectivity. This study demonstrates the potential of engineered P450BM3 mutants to catalyze highly *N*-oxidation selectivity reactions, thus expanding the enzyme's catalytic repertoire. Furthermore, it provides valuable insights into the molecular mechanisms governing

https://doi.org/10.1038/s41467-025-61773-3

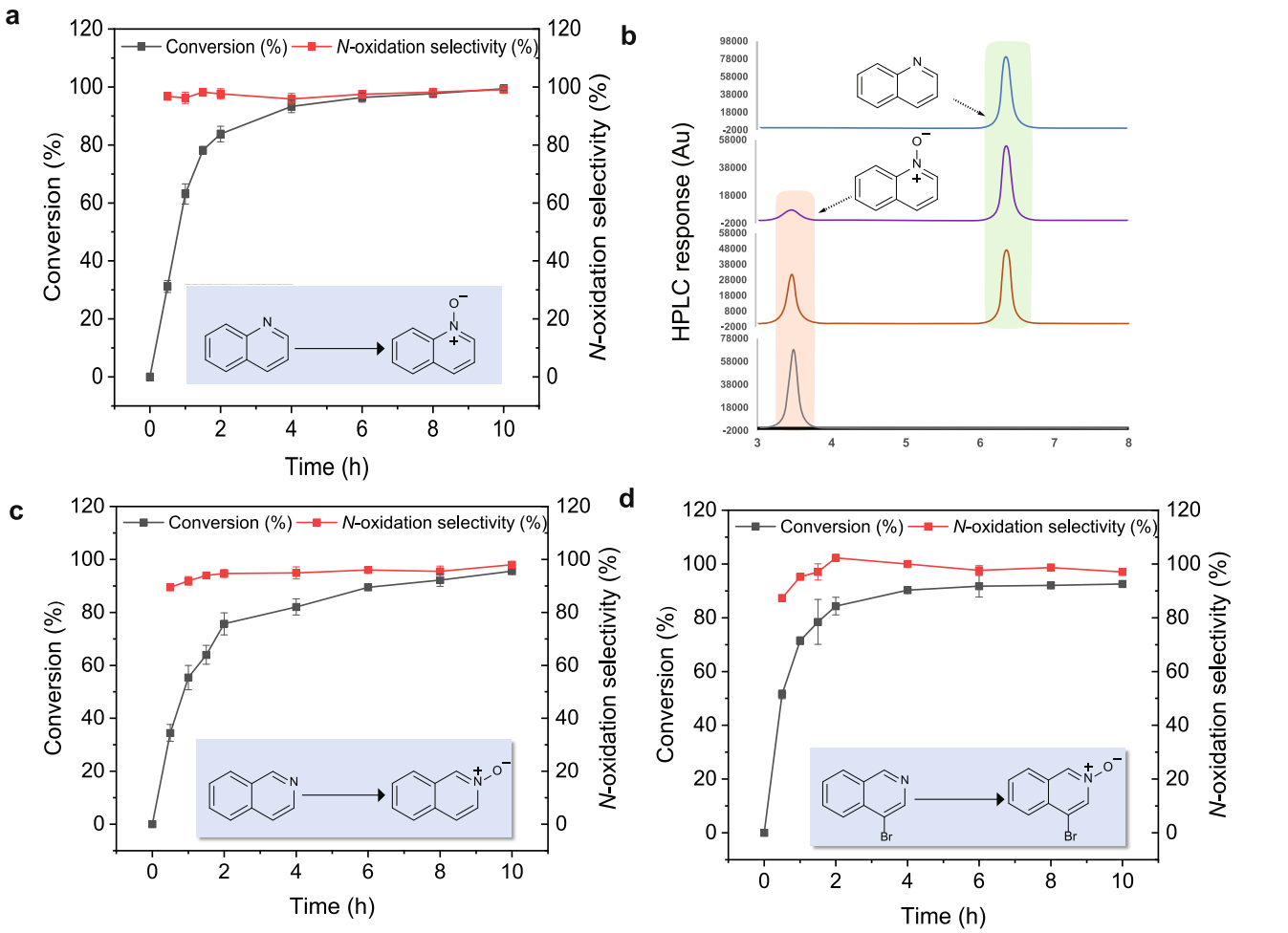

Fig. 9 | Scale-up reactions of *N*-oxidation catalyzed by the F87G/A264G/A328L mutant. Reaction Conditions: The reactions were conducted using 3 mM substrates in a K_2HPO_4-KH_2PO_4 buffer (50 mM, pH 8.0), along with a GDH-glucose-based cofactor regeneration system. The reactions were performed at 30 °C with stirring at 700 rpm and an oxygen supply rate of 0.5 mL/min. **a** Quinoline was used as the substrate. Data are presented as mean values ± SD over three independent biological repetitions. **b** HPLC analysis of the reaction process with quinoline as the substrate. **c** Isoquinoline was used as the substrate. Data are presented as mean values ± SD over three independent biological repetitions. **d** 4-Bromoisoquinoline was used as the substrate. Data are presented as mean values ± SD over three independent biological repetitions. Source data are provided as a Source Data file.

substrate recognition and *N*-oxidation selectivity in P450BM3, paving the way for future engineering efforts aimed at enhancing the enzyme's catalytic efficiency and substrate scope.

Methods

Chemicals, material, strain and plasmid

Quinoline was purchased from Aladdin. Isopropyl β-D-1-thiogalactopyranoside (IPTG, >99%), 5-aminolevulinic acid (5-ALA, >99%), and kanamycin (>99%) were bought from Bidepharm (Shanghai, China). Nicotinamide adenine dinucleotide phosphate (NADPH) and Nicotinamide adenine dinucleotide ($NADP^+$) were provided by Bangtai (Shenzhen, China). Tryptone and yeast extract were purchased from OXOID (Shanghai, China). Primer STAR Max DNA polymerase and restriction enzyme Dpn I were bought from Takara (Shanghai, China). The ClonExpress II One Step Cloning Kit was purchased from Vazyme. The Plasmid Miniprep Purification Kit and DNA Clean/Extraction Kit were ordered from Genemark (USA). The P450BM3 gene from *Bacillus megaterium* ATCC14581 (GenBank number: J04832) was synthesized and cloned into the pRSFDuet-1 vector. The gene encoding glucose dehydrogenase (GDH) was obtained from our laboratory. The expression vector used in this research was pRSFDuet-1, and the host strain was *Escherichia coli* BL21 (DE3).

Site-directed saturation mutagenesis and libraries screening

A modified QuikChange method was utilized to perform site-directed mutagenesis[60]. Saturation mutagenesis using NNK codon degeneracy (N: adenine/cytosine/guanine/thymine; K: guanine/thymine) was applied to encode all 20 canonical amino acids[50]. The primers used in this study are listed in Supplementary Table 3. For PCR amplification, a 50 µL solution was prepared, containing 25 µL of DNA polymerase mix (Primer Star, Takara Bio), 2.5 µL of 5′- and 3′-primers, 1 µL of DNA template, and 19 µL of sterile water. The PCR program consisted of 30 cycles at 98 °C for 15 seconds, 58 °C for 10 seconds, and 72 °C for 90 seconds. The PCR products were digested with the restriction enzyme Dpn I at 37 °C for 1 hour to eliminate the methylated DNA template. Subsequently, the products were recombined using the ClonExpress II One Step Cloning Kit. Finally, the PCR product was transformed into competent *E. coli* BL21 (DE3) cells.

The following procedure was employed to screen the mutant library: single colonies from the agar plates were randomly selected and transferred into 2.2 mL 96-deep-well plates containing 200 µL of LB medium supplemented with 50 µg/mL of kanamycin. The cultures were incubated at 37 °C with shaking at 220 rpm for 8 h. Subsequently, an aliquot of 50 µL was transferred to 400 µL of TB medium, also containing 50 µg/mL of kanamycin, and cultured at 37 °C in an orbital incubator shaker at 220 rpm. When the optical density at 600 nm

(OD_{600}) reached 0.8, the cells were induced with 0.2 mM IPTG and 0.5 mM 5-ALA. After 20 h of expression at 25 °C and 220 rpm, the cells were harvested by centrifugation at 4000 g for 10 min at 4 °C and washed twice with 500 μL of K_2HPO_4/KH_2PO_4 buffer (50 mM, pH 8.0). Supernatant was discarded, and the 96-well plates were stored at −80 °C.

The 96-deep-well plates were thawed at room temperature and lysed by resuspending them in 200 μL of K_2HPO_4/KH_2PO_4 buffer (50 mM, pH 8.0) containing a final concentration of 15 mg/L lysozyme at 37 °C with shaking at 220 rpm for 1 hour. The mutant library was screened in 96-well ELISA plates for NADPH depletion using quinoline as a substrate. The substrate was prepared as a 200 mM stock solution in DMSO. To 100 μL of the lysate supernatant, 80 μL of K_2HPO_4/KH_2PO_4 buffer (50 mM, pH 8.0) saturated with quinoline (final concentration of 1 mM) was added. The reaction was initiated by the addition of 20 μL of NADPH (final concentration of 1 mM), and NADPH oxidation was monitored at 340 nm for 10 min using a Spectramax Plus microtiter plate reader (Molecular Devices, Sunnyvale, CA). Promising candidates were selected, and their DNA plasmids were extracted to identify the mutations. The catalytic performance of the mutants was further confirmed by HPLC.

Expression of P450BM3 and biotransformation

E. coli BL21(DE3) harboring the pRSFDuet-1/P450BM3 plasmid and its mutants were incubated in 50 mL of LB liquid medium containing kanamycin (50 μg/mL) in a shaker at 37 °C. When the optical density at 600 nm (OD_{600}) reached 0.8, IPTG and 5-ALA were added to final concentrations of 0.2 mM and 0.5 mM, respectively, to induce protein expression at 25 °C for 20 h. The cell culture solutions were collected by centrifugation at 4000 g for 30 min, and the resulting pellets were suspended in 5 mL of K_2HPO_4/KH_2PO_4 buffer (50 mM, pH 8.0) and sonicated with a cycle of 3 seconds on and 7 seconds off for 60 cycles at 120 W. The mixture was then centrifuged at 12,000 g for 30 min at 4 °C, and the resulting brownish-red supernatant constituted the crude enzyme extract.

Quinoline was screened for oxidation using a variant library and a NADPH system in a 50 mM K_2HPO_4/KH_2PO_4 buffer, with a total reaction volume of 1 mL in 1.5 mL Eppendorf tubes. The substrate was introduced as a 200 mM stock solution in DMSO, achieving a final concentration of 1 mM, while 960 μL of crude enzyme was added to the mixture. The reaction was initiated by adding NADPH to reach a final concentration of 2 mM. After 16 h of shaking at 220 rpm and 30 °C, an equal volume of methanol was added to terminate the reaction. Samples were sonicated for 2 min and then separated by centrifugation at 12,000 g for 5 min. The supernatant was filtered through a 0.22 μm filter, and 20 μL was taken for HPLC analysis.

Purification of P450BM3 and determination of concentration

The crude enzyme solution was filtered using a 0.45 μm filter and subsequently loaded onto a nickel affinity column (Ni-NTA columns), which was prewashed with a binding buffer containing 50 mM imidazole. The target proteins were eluted with an elution buffer containing 250 mM imidazole, 500 mM NaCl, and 50 mM K_2HPO_4/KH_2PO_4, and then concentrated to a final volume of 1 mL using Amicon Ultra centrifugal filters (cut-off 50 kDa, at 4000 g for 30 min, repeated three times). The purified P450 proteins were analyzed using prefabricated protein gels (SurePAGE™, Bis-Tris, GenScript USA Inc.). Partial protein profiles are shown in Supplementary Fig. 5. The protein was shock-frozen with 10% glycerol and stored at −80 °C until further use. An aliquot was thawed at room temperature, and the enzyme concentration was determined by CO difference spectrum analysis prior to use.

Active P450 concentrations were measured using the CO-difference spectrum method. Two samples were prepared separately: in the first sample, 800 μL of K_2HPO_4/KH_2PO_4 buffer (50 mM, pH 8.0) containing P450BM3 wild-type and its mutants was mixed with 200 μL of 1 M sodium dithionite and then saturated with CO gas by introducing one bubble per second for 1 min. In the second sample, 800 μL of K_2HPO_4/KH_2PO_4 buffer (50 mM, pH 8.0) containing P450BM3 wild-type and its mutants was mixed with 200 μL of 1 M sodium dithionite as a blank control. The two samples were analyzed using a UV-spectrophotometer by scanning the wavelength from 400 nm to 500 nm. The active P450 content was calculated using the formula: CP450 (μM) = (ΔA450-ΔA490)/0.091 ($M^{-1}cm^{-1}$)[61].

Determination of NADPH consumption rates

Initial rates of NADPH consumption were measured using purified enzymes in a Spectramax Plus microtiter plate reader (Molecular Devices, Sunnyvale, CA). The total reaction system consisted of a quinoline solution (final concentration 1 mM) and 0.5 μM protein, which was incubated for 5 min in 50 mM K_2HPO_4/KH_2PO_4 buffer (pH 8.0) before initiating the reaction by adding 20 μL of NADPH (1 mM). The absorption at 340 nm was monitored throughout the experiment. Rates were corrected for background NADPH consumption measured in the absence of substrate. After 10 min, the reaction was terminated by adding an equal volume of methanol. The resulting supernatant was filtered through a 0.22 μm filter and analyzed by reversed-phase HPLC to determine the reaction rate. Each reaction was performed at least three times.

Measurement of the kinetic constants

The kinetic constants of the mutants were determined by measuring the reaction rates at varying concentrations of the substrate quinoline (ranging from 1 to 5 mM). The mixtures, containing 0.5 μM of enzymes and 1 mM of NADPH, were incubated at 30 °C for 10 min. Each reaction was performed at least three times. The kinetic measurements were analyzed using nonlinear regression to fit the Michaelis–Menten equation, allowing for the determination of *K*m and *k*cat.

Molecular dynamics simulations

The initial structure coordinates of the enzyme were taken from the Protein Data Bank (PDB ID: 1JPZ). The missing residues were completed using the Modeller program. In the previously suggested catalytic mechanism, the reaction is triggered by Compound I (Cpd I) species. The O atom above heme-iron was modeled as the oxo atom of Cpd I[62]. The protonation states of all titratable residues were assigned according to their p*K*a values calculated by the H + + procedure[63] and through visual inspection of local microenvironment (Supplementary Table 4). Overall, all Glu and Asp residues were deprotonated, while the Arg and Lys residues were protonated. The specific protonation states of histidines are determined by careful examination of their local environments in the crystal structure. His92, His100, His116, His171, His388, His408, His420, and His 426 were protonated at the epsilon nitrogen, while His361 were protonated at the delta nitrogen. The histidine residues His138, His236, His266, and His285 were doubly protonated at both the epsilon and delta nitrogen atoms[64] (Supplementary Fig. 5). The leap tools of the Amber package were used to give the coordinates of the missing hydrogen atoms. For further MD simulations, the general Amber force field (GAFF2) was utilized for both substrates[65]; The AMBER ff19SB force field was employed for the protein residues[66]. The parameters of Cpd I were taken from a previous study. Forty chloride (Cl^-) and thirty sodium (Na^+) ions were added to the protein surface with the leap tools to neutralize the total charge and maintain a physiological ionic strength of the system. The resulting system was solvated in a rectangular box filled with the OPC model waters extending up to a minimum distance of 12 Å from the enzyme's surface. Using the prepared system, molecular dynamics (MD) simulations were performed using the GPU version of AMBER24 package. The simulation protocol consisted of several stages:

First, a five-step energy minimization was conducted to remove bad contacts:

(1) Minimization of hydrogen atoms with 100.0 kcal/mol/$Å^2$ restraints on non-hydrogen atoms (5000 steps steepest descent followed by 5000 steps conjugate gradient)

(2) Minimization of water molecules and ions with 100.0 kcal/mol/Å^2 restraints on the protein and ligand (5000 steps steepest descent followed by 5000 steps conjugate gradient)
(3) Minimization with 50.0 kcal/mol/Å^2 restraints on the protein (5000 steps steepest descent followed by 5000 steps conjugate gradient)
(4) Minimization of side chains and solvent with 10.0 kcal/mol/Å^2 restraints on protein backbone atoms (5000 steps steepest descent followed by 5000 steps conjugate gradient)
(5) Finally, minimization of all atoms without any restraints (5000 steps steepest descent followed by 5000 steps conjugate gradient)

The system was then gradually heated from 0 to 100 K over 50 ps under NVT conditions, followed by heating from 100 to 300 K over 150 ps under NPT conditions, with 5.0–10.0 kcal/mol/Å^2 restraints on the protein backbone atoms. Density equilibration was performed for 250 ps under NPT conditions at 300 K and 1 atm pressure, maintaining the backbone restraints. The system was further equilibrated with gradually reducing restraints for 500 ps.

Finally, two-stage production MD simulations were performed. First, restrained classical MD simulations were conducted for 20 ns under NPT conditions at 300 K and 1 atm pressure, where distance restraints were maintained between the N atom of quinoline/isoquinoline and the O atom of CPDI according to the dist. RST file, with a force constant of 50 kcal·mol^{-1}·Å^{-2}. Subsequently, unrestrained MD simulations were performed for another 3 × 100 ns under the same conditions. For both stages, the temperature was controlled using the Langevin thermostat with a collision frequency of 5.0 ps^{-1}, and pressure was maintained using the Monte Carlo barostat with a relaxation time of 2.0 ps. The SHAKE algorithm was applied to constrain all bonds involving hydrogen atoms, allowing a time step of 2 fs. Periodic boundary conditions were employed with a 10 Å cutoff for non-bonded interactions. Coordinates were saved every 10 ps for analysis. Trajectory analysis was performed using the CPPTRAJ module. The binding free energy was calculated by the MM/GBSA (molecular mechanics/generalized Born surface area) method. The structures with converged RMSD values in the last 20 ns would be selected for further analysis. The interactions between amino acid residues were analyzed by using the "View Interactions" module of the protein structure visualization software Discovery Studio 4.0. The structure of proteins was analyzed using the visualization software PyMoL 3.1.

Scale-up reaction for the *N*-oxidation of quinoline, Isoquinoline, and 4-bromoisoquinoline

The scale-up reaction was conducted in a 50 mL system containing 30 mL of the lysate supernatant,100 mM glucose, 80 μM NADP$^+$, and 20 U/mL of glucose dehydrogenase (GDH). The reaction was initiated by adding 750 μL of substrate stock at a concentration of 200 mM in DMSO, resulting in a final concentration of 3 mM. The reaction was maintained at 30 °C and stirred at 700 rpm, while oxygen was supplied at a rate of 0.5 mL/min. The progress of the reaction was monitored through HPLC analysis.

Preparation of *N*-oxidation of *N*-heterocycles

A reaction was carried out in a 50 mL system 30 mL of the lysate supernatant, containing 100 mM glucose, 80 μM NADP$^+$, and 20 U/mL of glucose dehydrogenase (GDH). Substrate, including quinoline (**1a**), 4-chloroquinoline (**2a**), 3-methylquinoline (**3a**), 6-methoxyquinoline (**4a**), quinaldine (**6a**), isoquinoline (**7a**), 4-bromoisoquinoline (**8a**), 5-bromoisoquinoline (**9a**), 6-bromoisoquinoline (**10a**), 8-bromoisoquinoline (**11a**), 3-methylisoquinoline (**12a**), 2- picoline (**13a**), 4-picoline (**14a**) (each at a concentration of 200 mM in a stock solution of DMSO) were added to the reaction flask (500 μL for each substrate), The reaction was conducted at 30 °C, with stirring at 700 rpm and an oxygen supply of 0.5 ml/min for 16 h (for substrates **1a, 3a, 4a, 7a-12a**) and for 24 h (for substrates **2a, 6a, 13a-14a**). After the reaction, 50 mL of ethyl acetate was used three times to extract the products. The organic phases were combined, dried over anhydrous Na_2SO_4, and filtered. The organic solvent was then evaporated under a nitrogen blowdown. The resulting products were subsequently purified by flash chromatography on a silica gel column.

To isolate compounds **1b-4b, 6b**, and **7b-14b**, a mixture of n-hexane and ethyl acetate (EtOAc) in a 1:3 ratio was used as the eluent (Rf ≈ 0.25 for **1b**, 0.19 for **4b**, 0.26 for **6b**, 0.25 for **7b**, 0.13 for **10b**, 0.38 for **11b**, 0.16 for **13b**, 0.17 for **14b**). Additionally, a mixture of n-hexane and EtOAc in a 1:4 ratio was utilized as the eluent (Rf ≈ 0.44 for **2b**, 0.16 for **3b**, 0.31 for **8b**, 0.33 for **9b**, 0.20 for **12b**). The organic solvents from the collected fractions were evaporated under reduced pressure to yield the purified products **1b-4b** and **6b-14b**.

HPLC and LC-MS analysis

The analysis of substrates **1a-14a** and products **1b-14b** was conducted using an Agilent 1260 system equipped with a QS-C18 Plus column (5 μm, 4.6 × 250 mm). The HPLC program and chromatogram are detailed in Supplementary Table 5 and Supplementary Figs. 9– 22. The analysis of products **1b-7b** and **9b-11b** was performed using an Agilent 1290 system combined with a 6470 LC/TQ, utilizing an Eclipse Plus C18 RRHD column (1.8 μm, 2.1 × 50 mm). Mass spectra were generated using ESI$^+$ with a scan mass range of 50–300 m/z. The LC-MS program is as follows: 90% acetonitrile held for 3 min; 10% acetonitrile held for 4 min, with a flow rate of 0.40 mL/min and an injection volume of 0.50 μL.

NMR analysis

NMR spectra were recorded using a Bruker Avance NEO 600 Spectrometer with methanol-*d*4 or chloroform-*d* as the solvent (600 MHz for ^{1}H and 151 MHz for ^{13}C), with tetramethylsilane (TMS) as the internal standard (δ = 0 ppm). The data for NMR are reported in the conventional format: chemical shift (δ ppm), multiplicity (d = doublet, dd = doublet of doublets, t = triplet, q = quartet, m = multiplet), and coupling constant (Hz).

Reporting summary

Further information on research design is available in the Nature Portfolio Reporting Summary linked to this article.

Data availability

Authors declare that all data supporting the findings of this study are available within the paper and its Supplementary Information files. The PDB structure is used: 1JPZ. Source data are provided with this paper.

References

1. Enomoto, M., Kitagawa, W., Yasutake, Y. & Shimizu, H. Total synthesis of aurachins C, D, and L, and a structurally simplified analog of aurachin C. *Biosci. Biotechnol. Biochem.* **78**, 1324–1327 (2014).
2. Eliwa, D. et al. Papaverinol-N-Oxide: A microbial biotransformation product of papaverine with potential antidiabetic and antiobesity activity unveiled with in silico screening. *Molecules* **28**, 1420–3049 (2023).
3. Singh, J., Patel, R. I. & Sharma, A. Visible-light-mediated C-2 functionalization and deoxygenative strategies in heterocyclic *N*-Oxides. *Adv. Synth. Catal.* **364**, 2289–2306 (2022).
4. Huth, S. E., Stone, E. A., Crotti, S. & Miller, S. J. On the Ability of the N–O bond to support a stable stereogenic axis: peptide-catalyzed atroposelective N-Oxidation. *J. Org. Chem.* **88**, 12857–12862 (2023).
5. Zhang, G., Yang, K., Wang, S. H., Feng, Q. & Song, Q. L. N_2H_4–H_2O enabled umpolung cyclization of o-Nitro chalcones for the construction of quinoline *N*-Oxides. *Org. Lett.* **23**, 595–600 (2021).

6. Kohlpaintner, P. J. et al. Synthesis of aromatic *N*-Oxides using electrochemically generated peroxodicarbonate. *Org. Lett.* **26**, 1607–1611 (2024).
7. Liu, N., Shu, Y. J., Wang, B. Z., Li, X. Z. & Bi, F. Q. Cyclization: a useful approach for the synthesis of nitrogen heterocyclic *N*-Oxides. *Curr. Org. Chem.* **19**, 1896–1915 (2015).
8. Okuma, K., Seto, J. I., Nagahora, N. & Shioji, K. Chemoselective synthesis of quinoline N-oxides from 3-(2-nitrophenyl)-3-hydroxypropanones. *J. Heterocycl. Chem.* **47**, 1372–1378 (2010).
9. Winter, J., Prenzel, T., Wirtanen, T., Schollmeyer, D. & Waldvogel, S. R. Direct electrochemical synthesis of 2,3-disubstituted quinoline N-Oxides by cathodic reduction of nitro arenes. *Chem. Eur. J.* **29**, e202203319 (2023).
10. Brown, D. G. & Boström, J. Analysis of past and present synthetic methodologies on medicinal chemistry: where have all the new reactions gone?. *J. Med. Chem.* **59**, 4443–4458 (2016).
11. Solomon, V. R., Haq, W., Srivastava, K., Puri, S. K. & Katti, S. B. Design and synthesis of 3-[(7-chloro-1-oxidoquinolin-4-ylamino)alkyl]-1,3-thiazolidin-4-ones as antimalarial agents. *J. Enzym. Inhib. Med. Chem.* **28**, 1048–1053 (2012).
12. Larionov, O. V. et al. Insights into the mechanistic and synthetic aspects of the Mo/P-catalyzed oxidation of N-heterocycles. *Org. Biomol. Chem.* **12**, 3026–3036 (2014).
13. Chen, S. Y. et al. Continuous flow microreactor promoted the catalytic *N*-Oxidation reaction of pyridine derivatives. *Synthesis* **54**, 3999–4004 (2022).
14. Dyer, R. M. B., Hahn, P. L. & Hilinski, M. K. Selective heteroaryl *N*-Oxidation of amine-containing molecules. *Org. Lett.* **20**, 2011–2014 (2018).
15. Islam, A. N., Tofik, N. I., Tofik, B. B. & Mamedali, M. A. Oxidation of pyridine bases by hydrogen peroxide. *J. Chem. Chem. Eng.* **5**, 82–88 (2011).
16. Palav, A. et al. The m-CPBA – NH3(g) System: A Safe and Scalable Alternative for the Manufacture of (Substituted) Pyridine and Quinoline *N*-Oxides. *Org. Process Res. Dev.* **23**, 244–251 (2019).
17. Pleil, J. D. et al. Strategies for evaluating the environment–public health interaction of long-term latency disease: The quandary of the inconclusive case–control study. *Chem. Biol. Interact.* **196**, 68–78 (2012).
18. Sutherland, J. B., Freeman, J. P., Williams, A. J. & Cerniglia, C. E. N-Oxidation of quinoline and isoquinoline by *Cunninghamella elegans*. *Exp. Mycol.* **18**, 271–274 (1994).
19. Saeki, K., Takahashi, K. & Kawazoe, Y. Metabolism of mutagenicity-deprived 3-fluoroquinoline: comparison with mutagenic quinoline. *Biol. Pharm. Bull.* **16**, 232–234 (1993).
20. Saeki, K., Takahashi, K. & Kawazoe, Y. Potent mutagenic potential of 4-methylquinoline: metabolic and mechanistic considerations. *Biol. Pharm. Bull.* **19**, 541–546 (1996).
21. Dowers, T. S., Rock, D. A., Rock, D. A., Perkins, B. N. S. & Jones, J. P. An analysis of the regioselectivity of aromatic hydroxylation and N-oxygenation by cytochrome P450 enzymes. *Drug Metab. Dispos.* **32**, 328–332 (2004).
22. Real, A. M., Hong, S. & Pissios, P. Nicotinamide *N*-Oxidation by CYP2E1 in human liver microsomes. *Drug Metab. Dispos.* **41**, 550–553 (2013).
23. Dowers, T. S. & Jones, J. P. Kinetic isotope effects implicate a single oxidant for cytochrome P450-mediated *O*-dealkylation, *N*-oxygenation, and aromatic hydroxylation of 6-methoxyquinoline. *Drug Metab. Dispos.* **34**, 1288–1290 (2006).
24. Pogrányi, B. et al. Preparative-scale biocatalytic oxygenation of *N*-Heterocycles with a lyophilized peroxygenase Catalyst. *Angew. Chem. Int. Ed.* **62**, e202214759 (2023).
25. Hui, C. G. et al. Regio- and stereoselectivity in the $CYP450_{BM3}$-catalyzed hydroxylation of complex terpenoids: a QM/MM study. *Phys. Chem. Chem. Phys.* **22**, 21696–21706 (2020).
26. Sun, Y. D., Huang, X. Q., Osawa, Y. C., Chen, Y. E. & Zhang, H. The versatile biocatalyst of cytochrome P450 CYP102A1: structure, function, and engineering. *Molecules* **28**, 5353 (2023).
27. Li, A. T. et al. Regio- and stereoselective steroid hydroxylation at C7 by cytochrome P450 monooxygenase mutants. *Angew. Chem. Int. Edi.* **59**, 12499–12505 (2020).
28. Li, R. J., Tian, K. Y., Li, X. R., Gaikaiwari, A. R. & Li, Z. Engineering P450 monooxygenases for highly regioselective and active p-hydroxylation of m-Alkylphenols. *ACS Catal.* **12**, 5939–5948 (2020).
29. Ensari, Y., Santos, G. D., Ruff, A. J. & Schwaneberg, U. Engineered P450 BM3 and cpADH5 coupled cascade reaction for beta-oxo fatty acid methyl ester production in whole cells. *Enzym. Microb. Technol.* **138**, 109555 (2020).
30. Volz, T. J., Rock, D. A. & Jones, J. P. Evidence for two different active oxygen species in cytochrome P450 BM3 mediated sulfoxidation and N-dealkylation Reactions. *J. Am. Chem. Soc.* **124**, 9724–9725 (2020).
31. Morita, I. et al. Exploiting a C–N Bond Forming Cytochrome P450 Monooxygenase for C–S Bond Formation. *Angew. Chem. Int. Ed.* **59**, 3988–3993 (2020).
32. Steck, V., Kolev, J. N., Ren, X. & Fasan, R. Mechanism-guided design and discovery of efficient cytochrome P450-derived C-H amination biocatalysts. *J. Am. Chem. Soc.* **142**, 10343–10357 (2020).
33. Wang, C. E., Wu, P., Wang, Z. F. & Wang, B. J. The molecular mechanism of P450-catalyzed amination of the pyrrolidine derivative of lidocaine: insights from multiscale simulations. *RSC Adv.* **11**, 27674–27680 (2021).
34. Wang, J. B. et al. P450-BM3-catalyzed sulfoxidation versus hydroxylation: a common or two different catalytically active species?. *J. Am. Chem. Soc.* **142**, 2068–2073 (2020).
35. Zhou, H. Y. et al. Chemo- and regioselective dihydroxylation of benzene to hydroquinone enabled by engineered cytochrome P450 monooxygenase. *Angew. Chem. Int. Ed. Edi.* **58**, 764–768 (2019).
36. Carmichael, A. B. & Wong, L. L. Protein engineering of *Bacillus megaterium* CYP102 -: The oxidation of polycyclic aromatic hydrocarbons. *Eur. J. Biochem.* **268**, 3117–3125 (2001).
37. Ariyasu, S. et al. Catalytic oxidation of methane by wild-type cytochrome P450BM3 with chemically evolved decoy molecules. *ACS Catal.* **13**, 8613–8623 (2023).
38. Farinas, E. T., Schwaneberg, U., Glieder, A. & Arnold, F. H. Directed evolution of a cytochrome P450 monooxygenase for alkane oxidation. *Adv. Synth. Catal.* **343**, 601–606 (2001).
39. Li, A. T. et al. Whole-cell-catalyzed multiple regio- and stereoselective functionalizations in cascade reactions enabled by directed evolution. *Angew. Chem. Int. Ed. Edi.* **55**, 12026–12029 (2016).
40. Acevedo-Rocha, C. G. et al. P450-catalyzed regio- and diastereoselective steroid hydroxylation: efficient directed evolution enabled by mutability landscaping. *ACS Catal.* **8**, 3395–3410 (2018).
41. Chen, W. Y., Fisher, M. J., Leung, A., Cao, Y. & Wong, L. L. Oxidative diversification of steroids by nature-inspired scanning glycine mutagenesis of P450BM3 (CYP102A1. *ACS Catal.* **10**, 8334–8343 (2020).
42. Venkataraman, H. et al. A single active site mutation inverts stereoselectivity of 16-hydroxylation of testosterone catalyzed by engineered cytochrome P450 BM3. *ChemBioChem* **13**, 520–523 (2012).
43. Wang, Z. W. et al. How the conformational movement of the substrate drives the regioselective C – N bond formation in P450 TleB: insights from molecular dynamics simulations and quantum mechanical/molecular mechanical calculations. *J. Am. Chem. Soc.* **145**, 7252–7267 (2023).
44. Diao, W. W. et al. Preorganized internal electric field powers catalysis in the active site of uracil-DNA glycosylase. *ACS Catal.* **12**, 12488–12499 (2022).
45. Diao, W. W., Farrell, J. D., Wang, B. J., Yu, F. F. & Wang, Z. F. Preorganized internal electric field promotes a double displacement mechanism for the adenine excision reaction by adenine DNA glycosylase. *J. Phys. Chem. B* **127**, 8551–8564 (2023).

46. Dubey, K. D., Stuyver, T., Kalita, S. & Shaik, S. Solvent organization and rate regulation of a menshutkin reaction by oriented external electric fields are revealed by combined MD and QM/MM calculations. *J. Am. Chem. Soc.* **142**, 9955–9965 (2020).
47. Champness, N. R. The future of metal–organic frameworks. *Dalton Trans.* **40**, 10311–10315 (2011).
48. Whitehouse, C. J. C. et al. A highly active single-mutation variant of $P450_{BM3}$(CYP102A1). *ChemBioChem* **10**, 1654–1656 (2009).
49. Whitehouse, C. J. C. et al. Structural basis for the properties of two single-site proline mutants of CYP102A1 ($P450_{BM3}$). *ChemBioChem* **11**, 2549–2556 (2010).
50. Reetz, M. T., Kahakeaw, D. & Lohmer, R. Addressing the numbers problem in directed evolution. *ChemBioChem* **9**, 1797–1804 (2008).
51. Whitehouse, C. J. C., Bell, S. G. & Wong, L. L. $P450_{BM3}$ (CYP102A1): connecting the dots. *Chem. Soc. Rev.* **41**, 1218–1260 (2012).
52. Roberts, A. G. et al. The role of cytochrome P450 BM3 phenylalanine-87 and threonine-268 in binding organic hydroperoxides. *BBA-Gen. Subj.* **1860**, 669–677 (2016).
53. Seifert, A. et al. Rational design of a minimal and highly enriched CYP102A1 mutant library with improved regio-, stereo- and chemoselectivity. *Chembiochem* **10**, 853–861 (2009).
54. Reetz, M. T., Bocola, M., Carballeira, J. D., Zha, D. X. & Vogel, A. Expanding the Range of Substrate Acceptance of Enzymes: Combinatorial Active-Site Saturation Test. *Angew. Chem. Int. Edi.* **44**, 4192–4196 (2005).
55. Qu, G., Li, A. T., Acevedo-Rocha, C. G., Sun, Z. T. & Reetz, M. T. The Crucial Role of Methodology Development in Directed Evolution of Selective Enzymes. *Angew. Chem. Int. Edi.* **59**, 13204–13231 (2020).
56. Richard, L. et al. Quantum Mechanics/Molecular Mechanics Modeling of Regioselectivity of Drug Metabolism in Cytochrome P450 2C9. *J. Am. Chem. Soc.* **135**, 8001–8015 (2013).
57. Harder, M., Kuhn, B. & Diederich, F. Efficient Stacking on Protein Amide Fragments. *ChemMedChem* **8**, 397–404 (2013).
58. Pierce, A. C., Sandretto, K. L. & Bemis, G. W. Kinase inhibitors and the case for CH…O hydrogen bonds in protein–ligand binding. *Proteins* **49**, 567–576 (2002).
59. Dembitsky, V. M., Gloriozova, T. A. & Poroikov, V. V. Naturally occurring plant isoquinoline N-oxide alkaloids: Their pharmacological and SAR activities. *Phytomedicine* **22**, 183–202 (2015).
60. Zheng, L., Baumann, U. & Reymond, J. L. An efficient one-step site-directed and site-saturation mutagenesis protocol. *Nucleic Acids Res.* **32**, e115 (2004).
61. Omura, T. & Sato, R. The carbon monoxide-binding pigment of liver microsomes: I evidence for its hemoprotein nature. *J. Biol. Chem.* **239**, 2370–2378 (1964).
62. Shahrokh, K., Orendt, A., Yost, G. S. & Cheatham, T. E. III Quantum mechanically derived AMBER-compatible heme parameters for various states of the cytochrome P450 catalytic cycle. *J. Comput. Chem.* **33**, 119–133 (2011).
63. Anandakrishnan, R., Aguilar, B. & Onufriev, A. V. H++3.0: automating p K prediction and the preparation of biomolecular structures for atomistic molecular modeling and simulations. *Nucleic Acids res* **40**, W537–W541 (2012).
64. Zhang, H. H. & Hirao, H. Mechanism of Regio-and Enantioselective Hydroxylation of Arachidonic Acid Catalyzed by Human CYP2E1: A Combined Molecular Dynamics and Quantum Mechanics/Molecular Mechanics Study. *J. Chem. Inf. Model.* **65**, 2080–2092 (2025).
65. Wang, J. M., Wolf, R. M., Caldwell, J. W., Kollman, P. A. & Case, D. A. Development and testing of a general amber force field. *J. Comput. Chem.* **25**, 1157–1174 (2004).
66. Tian, C. et al. ff19SB: amino-acid-specific protein backbone parameters trained against quantum mechanics energy surfaces in solution. *J. Chem. Theory Comput.* **16**, 528–552 (2019).

Acknowledgements

This work was supported by the National Key Research and Development Program of China (No. 2019YFA0905000) to J.P.W., the National Natural Science Foundation of China (No. 22308317) and the "Pioneer" and "Leading Goose" R&D Program of Zhejiang (No. 2024C03013) to W.L.Z. The authors also would like to thank iBioFoundry and Core Facility at the Institute for Intelligent Bio/Chem Manufacturing, and Zhejiang Key Laboratory of Intelligent Manufacturing for Functional Chemicals, ZJU-Hangzhou Global Scientific and Technological Innovation Center.

Author contributions

L.Y. conducted the entire experimental operation, data collation and manuscript writing. Z.J.P. designed the MD analysis method and perform calculation and data analysis. L.Y. and Z.J.P. contributed equally to this work J.P.W. conducts project administration, paper review and editing, and funding acquisition. X.F.L. carried out enzyme expression and purification and conducted the data visualization. Z.W. participate in the calculation and analysis of MD. H.R.Y. conducted experimental method guidance and review. L.W.W. participated in scale-up experiments and optimized reaction conditions Y.M. and G.X. contributed synthesis for chemicals and materials. L.R.Y. conducts project administration, and funding acquisition. J.P.W. and W.L.Z. conceived of the project and designed the study. The manuscript was written by L.Y. and edited and approved by all authors.

Competing interests

The authors declare no competing interests.

Additional information

Supplementary information The online version contains supplementary material available at https://doi.org/10.1038/s41467-025-61773-3.

Correspondence and requests for materials should be addressed to Wenlong Zheng.

Peer review information *Nature Communications* thanks Aitao Li and Zhanfeng Wang for their contribution to the peer review of this work. A peer review file is available.